

Synchrotron and SSC Emission and the Blast-Wave Model of Gamma-Ray Bursts

James Chiang¹ and Charles D. Dermer

E. O. Hulburt Center for Space Research, Code 7653, Naval Research Laboratory, Washington DC 20375-5352

ABSTRACT

We investigate the dynamics and radiation from a relativistic blast-wave which decelerates as it sweeps up ambient matter. The bulk kinetic energy of the blast-wave shell is converted into internal energy by the process of accreting external matter. If it takes the form of non-thermal electrons and magnetic fields, then this internal energy will be emitted as synchrotron and synchrotron self-Compton radiation. We perform analytic and numerical calculations for the deceleration and radiative processes and present time-resolved spectra throughout the evolution of the blast-wave. We also examine the dependence of the burst spectra and light curves on various parameters describing the magnetic field and non-thermal electron distributions. We find that for bursts such as GRB 910503, GRB 910601 and GRB 910814, the spectral shapes of the prompt gamma-ray emission at the peaks in νF_ν strongly constrain the magnetic fields in these bursts to be well below ($\lesssim 10^{-2}$) the equipartition values. These calculations are also considered in the context of the afterglow emission from the recently detected gamma-ray burst counterparts.

1. Introduction

The recent Beppo-SAX observations of fading X-ray afterglows coincident with the positions of gamma-ray bursts GRB 970228 (Costa et al. 1997) and GRB 970508 (Piro et al. 1998) have led to the first identifications of possible burst counterparts in the optical wave band (van Paradijs et al. 1997; Djorgovski et al. 1997). In the optical spectrum associated with the latter burst, absorption lines have been detected with a redshift of $z = 0.835$ providing, for the first time, direct evidence for a gamma-ray burst at cosmological distances (Metzger et al. 1997). The gamma-ray fluence of GRB 970508 measured by BATSE is $\sim 3 \times 10^{-6}$ erg cm⁻² (Kouveliotou et al. 1997). Therefore, if the absorption line measurements give a lower limit on the redshift of the burst, this implies an isotropic burst energy of $> 10^{51}$ erg s⁻¹. An impulsive event releasing this amount of energy in a compact region naturally leads to a fireball and thence to a relativistic blast-wave.

¹NAS/NRC Research Associate

Blast-wave models for gamma-ray bursts have been examined previously in the literature in several contexts. The most extensive body of work on this topic has been produced by Mészáros, Rees and collaborators (e.g., Mészáros & Rees 1992a; Rees & Mészáros 1992; Mészáros, Laguna & Rees 1993; Wijers, Rees & Mészáros 1997; Panaitescu & Mészáros 1998a, 1998b; et al.). Other recent papers include Sari & Piran (1995), Vietri (1997), Waxman (1997), and Katz & Piran (1997). The basic fireball/blast-wave model consists of some triggering event—either coalescing neutron stars or black holes (Mészáros & Rees 1992b) or the collapse of a massive star (Paczynski 1998) or a failed type II supernova (Woosley 1993)—depositing a large amount of energy, $E_0 \sim 10^{51}$ – 10^{55} ergs, in a small region with radius $r_0 \sim 10^6$ – 10^7 cm. Because of the unavoidable presence of baryonic material, it is expected that the initial fireball energy will be transformed into kinetic energy of these baryons rather than escape as radiation. This material expands until the internal motions of the baryons become sub-relativistic in the co-moving frame of the material, at which point it forms a cold shell with bulk Lorentz factor $\Gamma_0 \simeq E_0/M_0c^2$, where M_0 is the rest mass of the contaminating baryons.

This shell continues to expand freely into the surrounding ambient medium until the integrated momentum impulse upon the shell by the swept-up matter is equal to the rest mass of the original material, $\Gamma_0 4\pi r_d^3 \rho_{\text{ext}}/3 \approx M_0$ where ρ_{ext} is the mass density of the external medium. This defines the so-called deceleration radius r_d (Rees & Mészáros 1992). Beyond this radius, the shell can no longer be regarded as freely expanding, and the bulk kinetic energy of the blast-wave begins to be reconverted into internal energy. If this internal energy is radiated promptly, then the deceleration of the blast-wave shell can be approximately described by $\Gamma(r) \propto r^{-3}$, and the expansion is said to be in the radiative regime. On the other hand, if the internal energy is radiated on a time scale which is long compared to the expansion time scale, then the expansion is in the non-radiative regime, and $\Gamma(r) \propto r^{-3/2}$. In either case, for large initial Lorentz factors, $\Gamma_0 \sim 10^2$ – 10^3 , relativistic effects (e.g., Rees 1966) compress the time scale for the radiation such that the bulk of the blast-wave energy is emitted in the first tens of seconds in the observer’s frame following the initial detonation event, thus producing the observed gamma-ray burst.

Several authors have pointed out that well after the prompt gamma-ray burst event the blast-wave shell will continue to decelerate and radiate (Vietri 1997; Waxman 1997). The recent detections by the X-ray, optical and radio communities of the aforementioned fading X-ray, optical and radio counterparts within the error boxes of GRBs appear to support this picture. Furthermore, model estimates of the temporal decay of these transients yield time-dependencies which agree with those observed, $F_\nu \sim t^{-1}$ (Wijers et al. 1997); and for the one of the bursts for which optical data are available (GRB 970508), the optical spectral index is consistent with synchrotron emission from a power-law distribution of electrons, $dN/d\gamma \propto \gamma^{-p}$ with $p \simeq 2$ – 2.3 (Djorgovski et al. 1997) indicating, for example, a shock-accelerated electron population.

Despite the successes of the blast-wave model in accounting for the prompt burst properties and its prediction of fading afterglows, several important theoretical questions must be addressed in order to have a reasonably complete model:

- What is the nature of the coupling between the electrons, protons and magnetic field (Panaitescu & Mészáros 1998b)? To what extent can these components be in equipartition given that only the electrons can efficiently radiate away their energy?
- How does the magnetic field change as the blast-wave decelerates? If it is initially formed through equipartition processes, but is not strongly coupled to the non-thermal electron energy density, how does it evolve?
- What is the nature of the acceleration mechanism? Are the electrons energized by repeated diffusion across the shocks themselves or by gyroresonant scattering with disturbances in the post-shock turbulent MHD fluid?
- What is the proper form for the injected electron energy distributions? Is it well described by a typical power-law spectrum? If so, what determines the characteristic energies of the particles?

In order to begin to address these questions, it is worthwhile to go beyond the simple, though useful, back-of-the-envelope estimates which have generally prevailed in the literature thus far. In this paper, we present a detailed calculation of the blast-wave deceleration and the evolution of the magnetic fields and electron distributions under various assumptions relevant to the above issues. We compute model light curves and spectra and use the available afterglow data to help discriminate between the various options. The format of the paper is as follows: In § 2, we describe the basic dynamics of an impulsively driven blast-wave which decelerates by accretion of ambient material. In § 3, we discuss the physical processes responsible for producing the observed radiation including prescriptions for magnetic field generation, the formation of non-thermal particle distributions and the relevant radiation processes. The numerical procedures for computing the deceleration of the blast-wave and the integration of the blast-wave shell emission are described in § 4. Model spectra and light curves for gamma-ray bursts are presented and analyzed in § 5. Lastly, in § 6, we discuss these results, explore prospects for further research and present our conclusions.

2. Deceleration of Impulsively Driven Blast-Waves

We assume that a shell of material, with initial proper mass M_0 , is injected with a bulk Lorentz factor Γ_0 and that its subsequent deceleration is determined by energy and momentum conservation as it accretes mass in the form of matter and internal energy from the ambient medium and loses inertia via radiative processes such as synchrotron or inverse Compton emission. The internal energy of the material is assumed to be initially negligible compared to its rest mass energy. This corresponds to a time well after the random internal energy of the initial fireball has been converted into the bulk kinetic energy of the spherically expanding shell. We model the blast-wave as having a cross-sectional area which is a function of the distance traveled r . This functional dependence can be parametrized as a power-law: $A(r) = A_0(r/r_0)^a = 4\pi f_b r^a$ where r_0 and A_0 are the initial

radius and surface area of the blast-wave, respectively, and f_b is a collimation factor to account for possible asymmetry of the explosion. In the calculations presented throughout this paper, we consider a spherical blast-wave with $A(r) = 4\pi r^2$.

A straight-forward application of energy and momentum conservation gives the equation of motion of the blast-wave shell as it sweeps up ambient matter. We obtain the following expression (Blandford & McKee 1976):

$$\frac{d\Gamma}{dm} = -\frac{\Gamma^2 - 1}{M}, \quad (1)$$

where $\Gamma = \Gamma(r)$ is the bulk Lorentz factor of the material, $M = M(r)$ is the total mass including internal kinetic energy, $dm(r) = A(r)\rho(r)dr$ is the *rest* mass swept-up in a distance dr , and the distance traveled r is measured in the stationary frame of the explosion. This frame will be referred to hereafter as the lab frame.

2.1. Radiative and Non-radiative Limits

As the blast-wave shell decelerates, its bulk kinetic energy is converted to internal kinetic energy. If this internal energy is not radiated away then it makes a significant contribution to the inertia of the blast-wave shell. In this case, the mass M , in equation 1, is given by

$$M_{nr}(r) = M_0 + \int_{r_0}^r \Gamma(\tilde{r})A(\tilde{r})\rho(\tilde{r})d\tilde{r}, \quad (2)$$

where the subscript *nr* identifies this as the non-radiative case. In the radiative case, the internal kinetic energy is immediately lost, and the inertia of the blast-wave shell consists only of the rest mass:

$$M_r(r) = M_0 + \int_{r_0}^r A(\tilde{r})\rho(\tilde{r})d\tilde{r}. \quad (3)$$

Note that since any radiation is assumed to be isotropic in the co-moving frame of the blast-wave shell, the bulk Lorentz factor is unaffected by this radiation and equation 1 still applies.

In the radiative case, $dM_r = dm$, the equation of motion (eq. 1) is separable, and the resulting integrals are elementary. The solution is

$$\Gamma(r) = \frac{(M_r(r)/M_0)^2(\Gamma_0 + 1) + \Gamma_0 - 1}{(M_r(r)/M_0)^2(\Gamma_0 + 1) - \Gamma_0 + 1} \quad (4)$$

(Blandford & McKee 1976). In the non-radiative case, the deceleration is described by a pair of coupled ordinary differential equations:

$$\frac{d\Gamma}{dr} = -\frac{A(r)\rho(r)(\Gamma(r)^2 - 1)}{M_{nr}(r)}, \quad (5)$$

$$\frac{dM_{nr}}{dr} = \Gamma(r)A(r)\rho(r). \quad (6)$$

These equations also have an analytic solution. The general expression for the mass is

$$M_{nr}(r) = \left[M_0^2 + 2\Gamma_0 M_0 M_{sw}(r) + M_{sw}(r)^2 \right]^{1/2}, \quad (7)$$

where $M_{sw}(r) = \int_{r_0}^r d\tilde{r} A(\tilde{r}) \rho(\tilde{r})$ is the swept-up *rest* mass of the ambient material. The bulk Lorentz factor is given by

$$\Gamma(r) = \frac{M_{sw}(r) + \Gamma_0 M_0}{M_{nr}(r)}. \quad (8)$$

For a spherical blast-wave in a uniform external medium, $A(r)\rho(r) = 4\pi r^2 \rho_0$. For $r \gg r_0$, the mass of the blast-wave shell is given by

$$M_{nr}(r) = \left[M_0^2 + 2\Gamma_0 M_0 \frac{4\pi}{3} r^3 \rho_0 + \left(\frac{4\pi}{3} r^3 \rho_0 \right)^2 \right]^{1/2}; \quad (9)$$

and the bulk Lorentz factor is

$$\Gamma(r) = \frac{1}{M_{nr}(r)} \left[\frac{4\pi}{3} r^3 \rho_0 + \Gamma_0 M_0 \right]. \quad (10)$$

From the above expression for the mass in the non-radiative case, we identify three regimes for the evolution of the blast-wave depending on which of the three terms dominates in equation 9. For $M_0 > 2\Gamma_0 M_{sw}$,

$$M_{nr}(r) \approx M_0, \quad (11)$$

$$\Gamma(r) \approx \Gamma_0. \quad (12)$$

This regime corresponds to the initial period of free-expansion. For $2\Gamma_0 M_{sw} > M_0 > M_{sw}/2\Gamma_0$,

$$M_{nr}(r) \approx [2\Gamma_0 M_0 M_{sw}]^{1/2}, \quad (13)$$

$$\Gamma(r) \approx \Gamma_0 \left[\left(\frac{M_0}{2\Gamma_0 M_{sw}} \right)^{1/2} + \frac{1}{\Gamma_0} \left(\frac{M_{sw}}{2\Gamma_0 M_0} \right)^{1/2} \right] \quad (14)$$

$$\propto r^{-3/2}. \quad (15)$$

Here we recover the familiar power-law $r^{-3/2}$ dependence of the bulk Lorentz factor which is often quoted for a non-radiative relativistic blast-wave decelerating in a uniform medium. Finally, when $M_{sw} > 2\Gamma_0 M_0$ the bulk motion of the blast-wave is non-relativistic, and we have

$$M_{nr}(r) \approx M_{sw}(r), \quad (16)$$

$$\Gamma(r) \approx 1 + \Gamma_0 \frac{M_0}{M_{sw}(r)}. \quad (17)$$

The velocity of the blast-wave inferred in this limit, using the approximation $\Gamma \simeq 1 + \beta^2/2$, is $\beta = \sqrt{\Gamma_0 M_0 / M_{sw}} \propto r^{-3/2}$, which agrees with the adiabatic solution for non-relativistic blast-waves (Lozinskaya 1992).

Energy conservation gives the rate of accreted kinetic energy as a function of time in the lab frame:

$$\frac{dE}{dt} = c^3 A(r) \rho(r) \beta (\Gamma^2 - \Gamma). \quad (18)$$

This expression follows directly from the equation of motion (eq. 1) and therefore applies regardless of whether the blast-wave is radiative or non-radiative. Since the above quantity is a Lorentz invariant, it also gives the injected power in the co-moving frame of the blast-wave (Blandford & McKee 1976).

2.2. Partially Radiative Regimes

In general, the evolution of the blast-wave shell will be intermediate between the radiative and non-radiative limits. If we denote the radiated power in the co-moving frame as dE_{rad}/dt , then the relativistic mass of the material is

$$M(r) = M_0 + \int_{r_0}^r d\tilde{r} \Gamma(\tilde{r}) \rho(\tilde{r}) A(\tilde{r}) - \int_0^t d\tilde{t} \frac{1}{c^2} \frac{dE_{\text{rad}}}{d\tilde{t}}, \quad (19)$$

where the latter integral is performed over co-moving time and represents the relativistic mass lost to radiation. Converting to the lab frame coordinate using $d\tilde{r} = c\beta\Gamma d\tilde{t}$, and differentiating wrt r , we obtain a more general form for equation 6:

$$\frac{dM}{dr} = \Gamma(r) \rho(r) A(r) - \frac{1}{c^3 \beta(r) \Gamma(r)} \frac{dE_{\text{rad}}}{dt}. \quad (20)$$

This expression must be integrated numerically in conjunction with the equation of motion (eq. 1). The radiated power dE_{rad}/dt is determined by the co-moving particle distributions and the relevant energy loss mechanisms. We address these issues in the following sections.

3. Physical Processes

3.1. Particle Injection Distributions

We assume that some fraction, ξ_e , of the accreted kinetic energy is injected directly into non-thermal electrons. Energization of these electrons may occur via acceleration by shocks (see e.g., Ellison, Baring & Jones 1995) or by gyroresonant scattering with plasma-wave turbulence induced by the swept-up material (Dermer, Miller & Li 1996). However, since we do not model these processes in detail, we adopt a power-law injection spectrum for the electron momenta, $dN/dp \sim p^{-s}$. In terms of the initial electron Lorentz factors, γ_i , this injection spectrum per unit co-moving time is

$$\frac{dN}{d\gamma dt_i} = \frac{dN_0}{dt_i} \gamma_i (\gamma_i^2 - 1)^{(s+1)/2}. \quad (21)$$

Here the time-dependent normalization of the injection spectrum is given by the prescribed fraction of the power available as kinetic energy:

$$\frac{dN_0}{dt_i} = \frac{\xi_e dE/dt}{m_e c^2 \int_{\gamma_{i,\min}}^{\gamma_{i,\max}} (\gamma_i^2 - \gamma_i)(\gamma_i - 1)^{(s+1)/2} d\gamma_i}. \quad (22)$$

The minimum injected electron Lorentz factor in the co-moving frame should be at least as large as the bulk Lorentz factor of the blast-wave, $\gamma_{i,\min} = \Gamma$. However, if the electrons are in equipartition with the protons, then the lower cut-off for the electron distribution will be approximately the typical energy of the incident protons in the co-moving frame, $\gamma_{i,\min} = (m_p/m_e)\Gamma$ (Katz & Piran 1997; Panaitescu & Mészáros 1998a). We parametrize the uncertainty between these two extremes with a parameter η :

$$\gamma_{i,\min} = \eta \frac{m_p}{m_e} \Gamma(r_i). \quad (23)$$

The upper cut-off of the electron distribution is given by balancing the radiative losses with the power gained due to the acceleration. By balancing acceleration time scales for both shock and gyroresonant processes with synchrotron loss time scales, de Jager et al. (1996; see also de Jager & Harding 1992) argue that for a given magnetic field the maximum electron Lorentz factor is:

$$\gamma_{i,\max} \simeq 4 \times 10^7 (B/1 \text{ G})^{-1/2}. \quad (24)$$

3.2. Magnetic Field Prescriptions

At a minimum, the post-shock magnetic field will be that of the ambient external field, amplified by the compression ratio (~ 4 for a strong shock) and the Lorentz transformation to the co-moving frame: $B \sim 4\Gamma B_{\text{pre}} \sim 10^{-5}\Gamma$ Gauss. Here we have assumed an ambient magnetic field intensity typical for the ISM of a few μG . Even for bulk Lorentz factors of $\Gamma \sim 10^3$, this field strength is too low for the electrons to be radiatively efficient. Another source of the magnetic field energy is the remnant field which was created during the initial fireball event and which gets carried along with the expanding blast-wave material. However, if flux freezing holds, i.e., $r^2 B \sim \text{constant}$, the field energy will decrease in proportion with the internal energy of the contaminating baryons, and by assumption we only consider the shell after it has expanded to the point at which the shell material is cold in the co-moving frame, hence the remnant field energy density should also be negligible.

If gyroresonant processes mediate the approach to equipartition between the protons and electrons, then it follows that the magnetic field will also be in equipartition with the particles. In true equipartition, the bulk of the internal energy will be deposited in components which are themselves not efficient radiators, namely the protons and the magnetic field. However, if strong coupling exists between the electrons, protons and the magnetic field such that these components remain in equipartition even as the electrons efficiently radiate away their kinetic energy, then we

would expect the dynamics of the blast-wave to be in the radiative regime (Panaitescu & Mészáros 1998b). In practice, this would correspond to $\xi_e \approx 1$ since the electrons would then be able to tap all of the available internal energy of the blast-wave shell. If the coupling between the magnetic field and particles is weak, then we would expect the internal energy in the protons and magnetic field to remain in the blast-wave and the blast-wave dynamics should be intermediate between radiative and non-radiative. In either case, we would expect that the generated magnetic field energy density will be proportional to the energy density of the swept-up material. This implies a magnetic field of the form:

$$B = (32\pi\xi_B\rho_{\text{ext}})^{1/2}\Gamma c, \quad (25)$$

where we have assumed a compression ratio of 4. The parameter ξ_B contains all the uncertainties regarding particle-field coupling and the degree to which equipartition is achieved and maintained. In principle, ξ_B will change with time depending on the complicated plasma physics processes taking place within the blast-wave. However, we will treat it as a constant and address the implications of this simplification in our discussion below.

3.3. Radiation Processes

The radiation processes which we consider are synchrotron and synchrotron self-Compton. An expression for optically thin emission spectra for these processes are given by Dermer, Sturmer & Schlickeiser (1997) where they use a δ -function approximation for the synchrotron spectrum of a single electron which is centered at the cyclotron frequency and which is normalized by the total synchrotron power. When convolved with a smooth distribution of electron energies, this approximation provides a reasonably accurate representation of the optically thin synchrotron emissivity:

$$\begin{aligned} j_{\text{syn}}(\epsilon) &= \frac{dE}{dt dV d\epsilon d\Omega} \\ &\simeq \frac{c\sigma_T u_B}{6\pi\epsilon_B} \left(\frac{\epsilon}{\epsilon_B}\right)^{1/2} \frac{dN}{dV d\gamma} \left[\left(\frac{\epsilon}{\epsilon_B}\right)^{1/2} \right]. \end{aligned} \quad (26)$$

Here $\epsilon = h\nu/m_e c^2$, $\epsilon_B = B/B_{\text{crit}} = B/4.414 \times 10^{13}$ G, σ_T is the Thomson cross-section, and $dN/dV d\gamma$ is the electron distribution function. Unfortunately, this approximation breaks down at the end-points of the electron distribution. In order to obtain a more accurate photon spectrum, we apply a more sophisticated calculation (Crusius & Schlickeiser 1986; 1988) appropriate for an isotropic distribution of electrons. However, we note that since the sharp electron cut-offs are themselves approximations, the spectra and light curves due to electrons at these cut-offs should be regarded with caution.

Using a similar δ -function approximation, Dermer et al. (1997) also derive an expression for the first-order SSC emissivity in the Thomson regime:

$$j_{\text{SSC}}(\epsilon) \simeq \frac{c\sigma_T^2 u_B r_b \epsilon^{1/2}}{9\pi\epsilon_B^{3/2}} \int_{\epsilon_B}^{\min(\epsilon, 1/\epsilon)} d\tilde{\epsilon} \tilde{\epsilon}^{-1} \frac{dN}{dV d\gamma} \left[\left(\frac{\tilde{\epsilon}}{\epsilon_B}\right)^{1/2} \right] \frac{dN}{dV d\gamma} \left[\left(\frac{\epsilon}{\tilde{\epsilon}}\right)^{1/2} \right]. \quad (27)$$

The factor r_b comes from the characteristic escape time ($\sim r_b/c$) for synchrotron photons to leave a homogeneous spherical blob. In the case of a blast-wave shell we take r_b to be the thickness of the shell in the co-moving frame.

4. Numerical Procedures

4.1. Evolution of the Non-Thermal Particle Distributions

The non-thermal particle distribution is governed by the equation of continuity in energy space:

$$\frac{\partial}{\partial t} \left(\frac{dN}{d\gamma} \right) + \frac{\partial}{\partial \gamma} \left(\dot{\gamma} \frac{dN}{d\gamma} \right) = \frac{dN}{dt_i d\gamma_i}. \quad (28)$$

The losses consist of radiative losses due to synchrotron and synchrotron self-Compton emission and adiabatic losses:

$$\dot{\gamma} = \dot{\gamma}_{\text{rad}} + \dot{\gamma}_{\text{adi}} \quad (29)$$

$$= -\frac{1}{m_e c^2} \frac{4}{3} \beta^2 \gamma^2 c \sigma_T (u_B + u_{\text{syn}}(\gamma)) - \frac{\gamma}{3} \frac{\dot{V}}{V}. \quad (30)$$

The first term on the rhs corresponds to the radiative losses where u_{syn} is the energy density of the synchrotron photons which can be up-scattered by an electron with Lorentz factor γ in the Thomson limit:

$$u_{\text{syn}}(\gamma) = \int_0^{1/\gamma} m_e c^2 d\epsilon \epsilon \frac{dn_{\text{syn}}}{d\epsilon dt}. \quad (31)$$

Here $dn_{\text{syn}}/d\epsilon dt$ is the synchrotron photon number spectral density. The second term on the rhs of equation 30 is the expansion losses where V is the volume of the emitting material. However, since the relevant radiative loss time scales are much shorter than the expansion time scales, we neglect the adiabatic loss term. We also find that bremsstrahlung losses can be neglected compared to the synchrotron and SSC losses.

The evolution of the particle distribution is computed by integrating equation 28 using an implicit finite differencing scheme (Press et al. 1992):

$$\frac{N_{i+1j} - N_{ij}}{t_{i+1} - t_i} + \frac{\dot{\gamma}_{i+1j+1} N_{i+1j+1} - \dot{\gamma}_{i+1j} N_{i+1j}}{\gamma_{j+1} - \gamma_j} = Q_{ij}. \quad (32)$$

Here $N_{ij} = dN/d\gamma(t_i, \gamma_j)$, $\dot{\gamma}_{ij} = \dot{\gamma}(t_i, \gamma_j)$, and the source term, Q_{ij} , is the injection function given by equation 21. This implicit finite differencing scheme yields a tridiagonal system of equations which is readily inverted to give the electron distribution as a function of time. We note that the losses associated with the SSC term depend on the electron distribution function through u_{syn} and must be determined self-consistently. This is achieved by iteration until the electron distribution has converged.

4.2. Self-Consistent Dynamics

If the kinetic energy deposited in the electrons is immediately radiated, then equation 20 is equivalent to

$$\frac{dM}{dr} = \rho(r)A(r) [(\Gamma(r) - 1)(1 - \xi_e) + 1]. \quad (33)$$

In general, however, dE_{rad}/dt depends on all previous history of the accretion process through $dN/d\gamma$ and the integration of the equation of continuity (eq. 28), hence dE_{rad}/dt contains an implicit integral over r . We integrate equation 20 by taking time steps equal to the shortest energy loss time scale $\Delta t \sim (\gamma/\dot{\gamma})_{\text{min}}$, and for each of these steps, estimate dE_{rad}/dt using

$$\left(\frac{dE_{\text{rad}}}{dt}\right)_{t_i} = \frac{m_e c^2}{(\Delta t)_i} \int_1^\infty d\gamma \gamma \left[\left(\frac{dN}{d\gamma}\right)_{t_{i-1}} - \left(\frac{dN}{d\gamma}\right)_{t_i} \right], \quad (34)$$

where $t_i = t_{i-1} + \Delta t$ is the time of the i th step. The bulk Lorentz factor and total mass are then obtained by forward-stepping: $\Gamma_i = \Gamma_{i-1} + \Delta r(d\Gamma/dr)$ and $M_i = M_{i-1} + \Delta r(dM/dr)$, where $\Delta r = c\beta\Gamma\Delta t$. The estimate of the radiated power (eq. 34) from this simple forward-stepped integration is then used as input for a variable step-size Runge-Kutta integrator and the process is repeated until convergence. Only for very low magnetic fields, $\lesssim 10^{-3}$ of the equipartition value, are several additional iterations required in order to obtain convergence.

4.3. Computing the Observed Spectra from the Co-Moving Emissivities

Using the electron distribution function from the integration of the equation of continuity and the expressions for the synchrotron and SSC emissivities, we compute the radiation in the co-moving frame of the blast-wave shell. Because of light travel time effects, emission from the blast-wave shell at different lab frame times contributes to the observed flux at a given observer time. Hence, in the observer frame, the flux at any given time will consist of an integration of the emission over the course of the blast-wave expansion. If a shell element moves radially outward from the point of the explosion with velocity $c\beta(r)$ and at an angle $\theta = \cos^{-1}\mu$ with respect to the observer line-of-sight, then the time delay between radiation from this shell element at radius r and the initial explosion event is given by

$$t_{\text{obs}} = \frac{1}{c} \left[\int_0^r \frac{d\tilde{r}}{\beta(\tilde{r})} - r \cos \theta \right]. \quad (35)$$

The observed photon flux is

$$\begin{aligned} \left(\frac{dN}{dAd\epsilon dt d\Omega}\right)_{\text{obs}} &= \frac{1}{4\pi d_l^2} \int_0^\infty dr \int_{\text{shell}} dA \mu \left(\frac{dN}{dAd\epsilon dt d\Omega}\right)_{co} \delta(r - \tilde{r}(t_{\text{obs}}, \mu)) \\ &\times \left| \frac{d\epsilon_{co}}{d\epsilon_{\text{obs}}} \right| \left| \frac{dt_{co}}{dt_{\text{obs}}} \right| \left| \frac{d\Omega_{co}}{d\Omega} \right| \left| \frac{dA_{co}}{dA} \right|, \end{aligned} \quad (36)$$

where d_l is the luminosity distance to the blast-wave, the dA -integral is performed over the shell surface at radius r , the element of area is $dA = 2\pi r^2 d\mu$, and the factor of μ accounts for the projection of the surface area of the shell. Note that for convenience we have taken the redshift to be $z = 0$. It is straight-forward to include the appropriate number of $(1 + z)$ factors in the final expressions. The \tilde{r} in the δ -function satisfies the time delay equation (35) for given values of t_{obs} and μ . The transformation from the co-moving frame to the observer frame introduces a number of Jacobian factors, all of which are powers of the Doppler factor $\mathcal{D} = [\Gamma(1 - \beta\mu)]^{-1}$: $|d\Omega_{co}/d\Omega| = \mathcal{D}^2$, $|d\epsilon_{\text{obs}}/d\epsilon_{co}| = \mathcal{D}$, $|dt_{\text{obs}}/dt_{co}| = \mathcal{D}^{-1}$, and $|dA_{co}/dA| = 1$. The area is unchanged since the velocity of the shell is perpendicular to its surface. Explicitly including all these factors and using the fact that the emission is isotropic in the co-moving frame, we obtain

$$\left(\frac{dN}{dA d\epsilon dt d\Omega}\right)_{\text{obs}} = \frac{1}{4\pi d_l^2} \int_{-1}^1 \frac{1}{8\pi} \left[\frac{dN}{d\epsilon_{co} dt_{co}} \frac{\mu d\mu}{[\Gamma(1 - \beta\mu)]^2} \right]_{r=\tilde{r}(t_{\text{obs}}, \mu)}, \quad (37)$$

where $dN/d\epsilon_{co} dt_{co}$ is calculated from the expressions for the synchrotron (eq. 26) and synchrotron self-Compton (eq. 27) emissivities and the integration of the electron equation of continuity (eqs. 28 & 32).

At a time delay t_{obs} the apparent size of the afterglow image on the sky will be given by the maximum value of the quantity $\rho = r\sqrt{1 - \mu^2}$. Differentiating wrt μ and using the expression for constant time delay (eq. 35) this maximum occurs at $\beta = \mu$, so that $\rho_{\text{max}} = \tilde{r}/\Gamma(\tilde{r})$. The quantity \tilde{r} is found by solving the equation

$$\tilde{r}\beta(\tilde{r}) = \int_0^{\tilde{r}} \frac{d\tilde{r}}{\beta(\tilde{r})} - ct_{\text{obs}}. \quad (38)$$

For constant β , the solution is $\tilde{r} = c\Gamma^2\beta t_{\text{obs}}$ yielding the standard result $\rho_{\text{max}} = c\Gamma\beta t_{\text{obs}}$. For a blast-wave shell in a uniform external medium whose Lorentz factor can be described by $\Gamma = \Gamma_0$ for $r < r_d \equiv (3M_0/8\pi\Gamma_0\rho_0)^{1/3}$, and $\Gamma = \Gamma_0(r/r_d)^{-\zeta}$ for $r > r_d$, where $\zeta \simeq 3/2$ in the non-radiative case and $\zeta \simeq 3$ in the radiative case, as long as $\Gamma \gg 1$ and $t_{\text{obs}} > (2\zeta/(2\zeta + 1))t_{\text{obs},0}$ where $t_{\text{obs},0} = r_d/2\Gamma_0^2 c$, the apparent size is

$$\rho_{\text{max}} \simeq \frac{r_d}{\Gamma_0} \left[\frac{1}{2(\zeta + 1)} \left((2\zeta + 1) \frac{t_{\text{obs}}}{t_{\text{obs},0}} - 2\zeta \right) \right]^{(2\zeta+1)/(\zeta+1)}. \quad (39)$$

In the radiative and non-radiative cases, $(2\zeta + 1)/(\zeta + 1) = 4/7$ and $5/8$ respectively (cf. Waxman, Kulkarni & Frail 1997). For purposes of illustration, we take an intermediate value, $(2\zeta + 1)/(\zeta + 1) = 3/5$, and obtain

$$\rho_{\text{max}} \simeq 1.4 \times 10^{13} \left(\frac{\Gamma_0}{10^3}\right)^{-1/15} \left(\frac{E_0}{10^{51} \text{ ergs}}\right)^{2/15} \left(\frac{n_{\text{ext}}}{1 \text{ cm}^{-3}}\right)^{-2/15} \left(\frac{t_{\text{obs}}}{1 \text{ sec}}\right)^{3/5} \text{ cm}. \quad (40)$$

For the radio afterglow associated with GRB 970508, Frail et al. (1997) find that the decline of the 8.64 GHz flux variability due to interstellar scintillation implies a source size of $\rho_{\text{max}} \approx 10^{17}$ cm at $t_{\text{obs}} \approx 1$ month. Using equation 40 above, this observation is consistent with a spherical blast-wave

with initial energy $E_0 \sim 10^{51}$ ergs expanding in an external medium with density $n_{\text{ext}} \sim 1 \text{ cm}^{-3}$. However, the very weak dependence of ρ_{max} on Γ_0 , E_0 , and n_{ext} means that any of these parameters could vary by as much as two orders of magnitude and not substantially change this result. The significance of equations 39 & 40 is the dependence of the apparent size with time. For a sufficiently bright radio afterglow, the blast-wave hypothesis could be tested by measuring the time dependence of the amplitude of the radio scintillation to determine if it conforms with the above prediction for the apparent size as a function of time (Goodman 1997; Frail et al. 1997; Waxman et al. 1997).

5. Model Light Curves and Spectra

We test our implementation of the above calculations by comparing our computer program’s output with the analytic results presented by Dermer & Chiang (1998) for the case of a radiative blast-wave and a constant magnetic field. For these calculations, we use $\Gamma_0 = 300$, $B = 1 \text{ G}$, an injection index of $s = 2$, and the blast-wave is assumed to be radiative. Figure 1a shows the spectra, $\epsilon^2 dN/d\epsilon dt$, as seen by an observer at times $t_{\text{obs}} = 1, 10, 10^2, \dots$ seconds for the numerical (solid curves) and analytic (dashed) calculations. The vertical lines indicate radio (2.4 GHz, dotted), optical (1 eV, solid), X-ray (1 keV, dashed) and gamma-ray (1 MeV, dot-dashed) energies. In figure 1b, the light curves corresponding to these energies are plotted, with the results from the analytic calculation over-plotted as symbols. The agreement is reasonably good, and the discrepancies are due to the fact that the analytic calculations use $\Gamma(r) = \Gamma_0(r/r_d)^{-3}$ for the bulk Lorentz factor rather than equation 4, somewhat different expressions for the electron energy losses due to synchrotron radiation, the electron distribution function and the δ -function approximation for the synchrotron emissivity. In addition, the use of the finite-difference method for calculating the evolution of the electron energies results in less sharp features (e.g., rounded high energy cut-offs) in the distributions.

In the upper panel of figure 2, we plot the surface brightness in the radio waveband as a function of perpendicular distance, ρ , for this calculation. As before, a curve is shown for time delays $t_{\text{obs}} = 1, 10, 10^2, \dots$ seconds (plotted top to bottom). Each curve is computed as a function of observer angle $\theta = \cos^{-1} \mu$, thus the surface brightness is double-valued and turns around at ρ_{max} . The flat portion within ρ_{max} results from emission from the leading surface of the blast-wave shell, i.e., for $\theta \leq \Gamma(\tilde{r})$. In the lower panel, we plot ρ_{max} for each time delay, t_{obs} , along with the curve given by equation 39 using $E_0 = 10^{50}$ ergs, $\Gamma_0 = 300$, $n_{\text{ext}} = 1 \text{ cm}^{-3}$, and $\zeta = 3$.

An example of a more realistic calculation is shown in figure 3. In figure 3a, we plot as the solid curve the bulk Lorentz factor of the blast-wave shell as a function of distance from the central explosion. The initial Lorentz factor is $\Gamma_0 = 300$, the fireball energy is $E_0 = 10^{52}$ ergs, and the ambient density is $n_{\text{ext}} = 1 \text{ cm}^{-3}$. We use $\xi_B = 1$ and $\eta = 1$ for the minimum electron energy (eq. 23), and the index of the electron momentum distribution is $s = 3$. The radius at which the free-expansion phase ends and the deceleration phase begins is consistent with the analytic estimate of $r_d = (3E_0/8\pi m_p c^2 n_{\text{ext}} \Gamma_0^2) = 2 \times 10^{16} \text{ cm}$. The fraction of kinetic energy made available

for radiation by electrons is $\xi_e = 0.5$. Since this is less than unity, the evolution of the bulk Lorentz factor lies between the two limiting cases with $\Gamma(r) \propto r^{-1.9}$ for $r > r_d$. Figure 3b shows the photon spectra, including the synchrotron self-Compton component, at observed time delays $t_{\text{obs}} = 1, 10, 10^2 \dots$ seconds after the initial fireball event. The blast-wave radii corresponding to these times are indicated as dotted vertical lines in figure 3a.

At early times, the shape of the synchrotron part of these spectra can be inferred directly from the corresponding co-moving electron distributions at the leading surface of the blast-wave (i.e., at $\mu = 1$) since the bulk of the observed radiation originates from within a small angle $\sim 1/\Gamma$ around this region. These distributions are shown in figure 3c with the earlier distributions corresponding to the lower curves. The shapes of these distributions are determined by the momentum dependence of the particle energy loss rates and the shape of the injection spectra. The steep sections at high energies, above the break but below the high energy cut-off, are the power-law-injected electrons which have evolved to a cooled distribution with $dN/d\gamma \sim \gamma^{-(s-1)}$ (Dermer & Chiang 1998). The break energy (e.g., $\gamma_{\text{break}} \simeq 6 \times 10^5$ for the $t_{\text{obs}} = 1$ s curve) is the minimum injection energy corresponding to the leading part of the blast-wave, $\gamma_{\text{break}} \approx \gamma_{i,\text{min}} = \eta(m_p/m_e)\Gamma$, and the electrons with the smallest energies ($\gamma_{\text{min}} \simeq 10^2$) are those which were injected at early times with $\gamma_i = (m_p/m_e)\Gamma_0$ but which have cooled due to radiative losses. The flat sections at energies less than γ_{min} result from synchrotron cooling of continuously injected electron distributions which have sharp low energy cut-offs. The spectral shape, $dN/d\gamma \sim \gamma^{-2}$, is due to the energy dependence of the energy loss rate, $\dot{\gamma} \propto -\gamma^2$. This shape is independent of the injection power-law index and hence will be a generic feature of a synchrotron-cooled electron spectrum resulting from injection spectra with sharp lower cut-off injection energies. An analytic expression for this part of the spectrum can be obtained by treating the injection function as a δ -function at the minimum injection energy:

$$\frac{dN}{d\gamma_i dt_i} \rightarrow \frac{dN_0}{dt_i} \delta\left(\gamma_i - \eta \frac{m_p}{m_e} \Gamma_i\right) \int_{\gamma_{i,\text{min}}}^{\gamma_{i,\text{max}}} d\tilde{\gamma}_i \tilde{\gamma}_i^{-s}, \quad (41)$$

where $\Gamma_i = \Gamma(r_i)$, r_i is the radius at which this distribution is injected and the integral on the rhs sets the normalization. We find, in terms of observing time t_{obs} ,

$$\gamma^2 \frac{dN}{d\gamma} = \left(\frac{3\pi m_e \xi_e}{4\sigma_T m_p \xi_B \eta} \right) \frac{r_d^2}{\Gamma_0} \times \begin{cases} (t_{\text{obs}}/t_{\text{obs},0})^2 & t_{\text{obs}} \leq t_{\text{obs},0} \\ [(2\zeta + 1)(t_{\text{obs}}/t_{\text{obs},0}) - 2\zeta]^{(\zeta+2)/(2\zeta+1)} & t_{\text{obs}} > t_{\text{obs},0}. \end{cases} \quad (42)$$

This expression is valid for $s > 2$. The electron spectra implied by this expression, including the cooled high energy power-law distribution above the breaks at $\gamma_{i,\text{min}}$ and the estimated roll-overs at low energies, are plotted as dashed curves in figure 3c.

In figure 3b, the energy of the peak of the synchrotron spectrum corresponds to the break at high electron energies. These quantities are related by

$$\epsilon_{\text{peak}} \approx \frac{B}{B_{\text{crit}}} \gamma_{\text{break}}^2 \Gamma \quad (43)$$

$$\approx \frac{\sqrt{32\pi\xi_B m_p c^2 n_{\text{ext}} \Gamma^2}}{B_{\text{crit}}} \eta^2 \left(\frac{m_p}{m_e}\right)^2 \Gamma^3 \quad (44)$$

$$\approx 3 \times 10^{-8} \xi_B^{1/2} n_{\text{ext}}^{1/2} \eta^2 \Gamma^4 \quad (45)$$

(Katz & Piran 1997). Using this relation in conjunction with the expressions for the synchrotron spectrum (eq. 26) and the electron distributions (eq. 42), we find the temporal dependence of the peak of the synchrotron component:

$$\left(\epsilon^2 \frac{dN}{d\epsilon dt} \right)_{\text{peak}} \simeq 2\pi m_p c^2 n_{\text{ext}} \xi_e r_d^2 \Gamma_0^2 \times \begin{cases} (t_{\text{obs}}/t_{\text{obs},0})^2 & t_{\text{obs}} \leq t_{\text{obs},0} \\ [(2\zeta + 1)(t_{\text{obs}}/t_{\text{obs},0}) - 2\zeta]^{(2-2\zeta)/(2\zeta+1)} & t_{\text{obs}} > t_{\text{obs},0}. \end{cases} \quad (46)$$

Here we see that the maximum of the light curve of the peak energy occurs at $t_{\text{obs},0} = r_d/2c\Gamma_0^2$. We also note that the above expression is independent of the magnetic field equipartition parameter.

With an injection index of s yielding a power-law index for the cooled distribution of $p = s + 1$, the energy index of the corresponding synchrotron emission is $\alpha = s/2$ ($L_\nu \propto \nu^{-\alpha}$). Depending on the strength of the magnetic field, the energy index of the synchrotron spectrum just below ϵ_{peak} will be either $\alpha = 1/2$ or $-1/3$. If the field strength is well below equipartition, i.e., $\xi_B \ll 1$, then the cooling time will be very long, the electrons at the low energy cut-off will have little time to cool, the flat portion of the spectrum will be very narrow or non-existent, and the low energy spectrum will be that of a cut-off electron distribution: $j_{\text{syn}} \propto \epsilon^{1/3}$ (Katz 1994; Rybicki & Lightman 1979). This latter behavior is seen in the spectra of the bright bursts GRB 910503 and GRB 910814, while a softer transition region with $j_{\text{syn}} \propto \epsilon^{-1/2}$ between the harder $\alpha = -1/3$ section at lower energies and the peak in νF_ν may be present in the spectrum of GRB 910601 (Schaefer et al. 1998). This may indicate that the synchrotron cooling of this latter burst is relatively more efficient than that of the other two bursts.

More quantitatively, the location of the spectral peak and the shape of the spectrum above and below ϵ_{peak} place strong limits on the equipartition parameter ξ_B , the initial bulk Lorentz factor Γ_0 and the injection spectral index s . For $t_{\text{obs}} > t_{\text{obs},0}$, the lower cut-off electron Lorentz factor is

$$\gamma_{\text{min}} = \gamma_0 \left[1 + \gamma_0 \frac{a_0 t_0}{\zeta - 1} \left(1 - \left(\frac{r}{r_d} \right)^{1-\zeta} \right) \right]^{-1}, \quad (47)$$

where $a_0 = (16/3)c\sigma_T(m_p/m_e)n_{\text{ext}}\xi_B\Gamma_0^2$ and $\gamma_0 = \eta(m_p/m_e)\Gamma_0$. In deriving this expression, we assume that the particle injection is only significant once the blast-wave reaches the deceleration phase $r > r_d$. For a burst spectrum in which electron cooling is important at all electron energies, which occurs if $t_{\text{co}} \simeq 2\Gamma_0 t_{\text{obs}} < (\gamma/\dot{\gamma})_{\text{min}}$, the minimum electron Lorentz factor obeys

$$\gamma_{\text{min}} \leq \gamma_{i,\text{min}} = \eta \frac{m_p}{m_e} \Gamma \quad (48)$$

$$= \gamma_0 \left(\frac{r}{r_d} \right)^{-\zeta}. \quad (49)$$

Writing $r/r_d = 1 + (r - r_d)/r_d$ and expanding equations 47 & 49 to first order, we obtain $a_0 \gtrsim \zeta/\gamma_0 t_0$. In terms of the relevant model parameters,

$$\eta \xi_B \Gamma_0^{4/3} \gtrsim 0.09 E_{52}^{-1/3} n_1^{-2/3} \zeta, \quad (50)$$

where $E_{52} = E/10^{52}$ erg and $n_1 = n_{\text{ext}}/1 \text{ cm}^{-3}$. Using this expression in conjunction with equation 45, we find

$$\Gamma_0 \lesssim 2.6 \times 10^2 E_{52}^{1/20} n_1^{-1/20} \zeta^{-3/20} \eta^{-9/20} \epsilon_{\text{peak}}^{3/10} \quad (51)$$

$$\xi_B \gtrsim 5.5 \times 10^{-5} E_{52}^{-2/5} n_1^{-3/5} \zeta^{6/5} \eta^{-2/5} \epsilon_{\text{peak}}^{-2/5}. \quad (52)$$

Thus, for burst spectra peaking at ~ 1 MeV and for which electron cooling is important, we obtain an upper limit for the initial bulk Lorentz factor of ~ 300 . Remarkably, this upper limit depends only very weakly on the total burst energy and the density of the ambient medium. For bulk Lorentz factors less than the above limit, the equipartition fields will be sufficiently strong so that the energy spectral index just below ϵ_{peak} will be $\alpha = 1/2$ and there will be a break at even lower energies below which $\alpha = -1/3$.

Bulk Lorentz factors larger than the above limit are possible, but in these cases, the electrons will not be fully cooled. If the injection index is $s > 3$, then just above ϵ_{peak} the energy spectral index will be that of the uncooled power-law electron distribution, $\alpha = (s - 1)/2$. Furthermore, if the upper injection cut-off, $\gamma_{i,\text{max}}$, is sufficiently high, an additional spectral break of $\Delta\alpha = 1/2$ will exist at higher energies marking the transition between the cooled and uncooled electrons (Dermer & Chiang 1998). Such a break would manifest itself as curvature in the high energy tail above ϵ_{peak} . If the electron injection index is $s < 3$, then the peak in νL_ν may actually correspond to the transition between cooled and uncooled power-law electron distributions. More likely, however, the peak in νL_ν will correspond to the synchrotron emission from the electrons at the upper cut-off (unless this upper cut-off energy is very high). In this case, there will be a spectral break between $\alpha = -1/3$ and $\alpha = (s - 1)/2$ below the peak in νL_ν and an exponential cut-off above the peak (Rybicki & Lightman 1979). None of the bursts for which good spectra are available show an exponential cut-off above the νL_ν peak or a spectral index change of $\Delta\alpha = 1/2$ at the peak itself (Tavani 1996; Schaefer et al. 1998). In figure 4, we show burst spectra illustrating the various spectral shapes we have described.

The evolution of the electron distributions will also be reflected in the afterglow emission. In figure 3d, we show the light curves at radio, optical, X-ray, gamma-ray, and TeV (dot-dot-dot-dashed curve) energies. As with our earlier calculation, these energies are indicated by vertical lines in the figure 3b. As the low energy electron cut-off evolves downward due to cooling, the hard, low energy part of the synchrotron spectrum will also move downward in energy. The evolution of the bulk Lorentz factor as the blast-wave decelerates contributes to this effect as well. At lower observer energies, the light curve will peak later and the spectral index will get softer with time. However, the precise shape of the light curve in any given band is difficult to predict due to the uncertainties in the nature of the electron cut-off and the evolution of the magnetic field. The general trend of hard-to-soft evolution should nevertheless hold, even if only qualitatively. Once the blast-wave has evolved so that the emission of the cooled power-law electron distribution lies within the optical band-pass, a measurement of the electron distribution power-law index can be inferred from optical afterglow data. For the afterglow of GRB 970508, the optical energy spectral index is $\alpha \sim 0.7 \pm 0.3$

(Djorgovski et al. 1997), which is consistent with a cooled power-law distribution with $s = 1.4$. This value is quite different from the injection indices implied by the prompt gamma-ray emission of GRBs 910503, 910601 & 910814 (Schaefer et al. 1998). The energy spectral indices for the high energy tail of the prompt burst emission range from $\alpha = 1.3$ – 2.5 , corresponding to injection indices of $s = 2.6$ – 5 if these electrons are cooled and even larger values of $s = 3.6$ – 6 if they are not cooled (Tavani 1996).

In addition to the evolution of the electron distribution injection index, it is expected that the magnetic field will not stay at a constant fraction of its equipartition value. If there is some sort of time scale, τ_{eq} , for particle-field equipartition to obtain, then one might expect that $\xi_B \approx \tau_{eq}/t_0$ where $t_0 = r_d/c\Gamma_0$ is the dynamical time scale of the blast-wave expansion in the co-moving frame. From equation 45, bursts which peak at 1 MeV have weak magnetic fields with $\xi_B \approx 10^{-4}$ for $\Gamma_0 = 300$. This implies a rather long equipartition time scale of $\tau_{eq} \approx 2 \times 10^7$ s. Even for a non-radiative burst, this time scale is reached only after the burst has almost completely decelerated. Most likely, particle-field equilibration is a highly non-linear process and thus cannot be parametrized as a simple linear function of time. The lack of a proper theory describing such processes poses a major uncertainty in using the characteristics of the prompt gamma-ray burst to set model parameters for extrapolation of the behavior of the blast-wave to describe the emission at much later times.

Nonetheless, for purposes of illustration, we present a calculation which largely matches the observed properties of typical prompt GRB emission. In as much as the spectral slopes for GRBs below the νF_ν peak are consistent with $\alpha = -1/3$ (Schaefer et al. 1998), the limiting values of $\Gamma_0 = 260$ and $\xi_B = 5.5 \times 10^{-5}$ apply. These values also insure that for the prompt burst spectrum we have $\epsilon_{\text{peak}} \sim 1$ MeV. We have also set $E_0 = 10^{52}$ ergs, and used a compromise value for the injection index of $s = 3$. In figure 5, we show the results of a calculation for those parameters. The blast-wave is almost non-radiative, with $\zeta \simeq 1.6$. Despite the aforementioned uncertainties in the model, this calculation displays many of the properties which have been seen in actual bursts and their putative afterglows. In comparison with the calculation shown in fig. 3, it demonstrates the variety of afterglow behaviors which can be obtained.

In figure 5b, the gamma-ray emission in the prompt burst extends up to 1 GeV, well into the EGRET energy range (cf. Dingus 1995), the initial rises in the X-ray and optical light curves follow that of the prompt burst itself by $\sim 10^3$ s and $\sim 5 \times 10^4$ s, respectively. However, because of the steeper injection index implied by the prompt burst, the flux in the X-ray band decays as $\sim t^{-1.9}$, significantly faster than that measured for GRB 970508 (Piro et al. 1998). The optical light curve decays somewhat slower as $\sim t^{-1.3}$ since the optical emission corresponds to the flatter part of the spectrum near the peak in νL_ν . The prompt burst spectrum evolves from hard to soft, and its time scale is ~ 10 seconds. The radio light curve is rising as $\sim t^{0.3}$ and the radio spectral index is $\alpha = -1/3$. Furthermore, this model makes the prediction of TeV emission due to SSC processes which should peak at a time comparable to the peak in the X-rays.

6. Conclusions

In this paper, we have attempted a more realistic calculation of the dynamics and synchrotron and synchrotron self-Compton emission for the blast-wave model of gamma-ray bursts. By matching the detailed characteristics of burst spectra, we have found relations (eqs. 51 & 52) which place constraints on magnetic field strengths and bulk Lorentz factors. If these relations are to be believed, then burst data can have a significant impact on models of magnetic field generation in turbulent plasmas.

The apparent deficiencies of this calculation point towards areas of further research. In particular, the detailed temporal structure of individual bursts is not explicitly dealt with in this model. In the context of external shocks, it may be due to inhomogeneities in the external medium, or fluctuations in the electron injection and/or magnetic field equipartition parameters (Panaitescu & Mészáros 1998a). For $s > 3$, the generalized expression for the luminosity for energies $\epsilon \geq \epsilon_{\text{peak}}$ (eq. 46) is

$$\epsilon^2 \frac{dN}{d\epsilon dt} = 2\pi m_p c^2 \xi_e r^2 n_{\text{ext}}(r) \Gamma^2(r) (\epsilon/\epsilon_{\text{peak}})^\lambda \quad (53)$$

where $\lambda = (2 - s)/2$ applies for relatively strong magnetic fields $\xi_B \gtrsim 10^{-4}$ when the electrons just above the break are efficiently cooled and $\lambda = (3 - s)/2$ applies for relatively weak fields and uncooled electrons. From this expression we see that any burst light curve substructure must be due to variations in ξ_e and n_{ext} , and indirectly, due to variations in ξ_B through ϵ_{peak} (eq. 45).

Our treatment of the dynamics also ignores the structure of the shock region itself, and our approach essentially only considers the emission from the forward shock and neglects the reverse shock. Panaitescu & Mészáros (1998a) have performed calculations similar to our own, but from a hydrodynamical perspective, and found that the reverse shock only makes a significant contribution to the emission at optical and UV energies. Therefore, neglecting the reverse shock should not affect our results for the gamma-ray emission, but it could have a significant impact on the optical and radio afterglow emission. We also neglect the thickness, Δr , of the shock shell in integrating the emission for a given observer time t_{obs} . This should not be important at early times when $\Delta r = r_0/\Gamma_0^2$ (in the lab frame), but it could affect the afterglow emission at late times.

It is unlikely that the blast-wave itself is spherical. If the initial fireball is created by the coalescence of two compact objects, then the orbital plane defines a natural axis of symmetry along which the blast-wave will propagate (Mészáros & Rees 1992b). This sort of asymmetry could be accounted for in our model by a non-unity collimation factor, f_b . Furthermore, if the observer line-of-sight does not lie within the opening angle of the blast-wave cone, then other effects due to relativistic beaming and the gradual deceleration of the shock front would be introduced. In this respect, highly anisotropic blast-waves would share properties with relativistic jets in blazars.

This analogy can be taken even further by noting the similarity of the burst spectra we derive compared to that of gamma-ray blazars. Like our model spectra, the spectral energy distributions (SEDs) of these objects tend to have two peaks, one in the UV–X-ray range and one at gamma-ray

energies. If the lower peak in blazar SEDs is due to synchrotron emission and corresponds to the ~ 1 MeV peak in gamma-ray bursts, we can apply a similar analysis as we have discussed above to derive bulk Lorentz factors and equipartition parameters for blazars. In particular, the recent ASCA observations of Mrk 421 (Takahashi et al. 1996) provide sufficient information to get actual values rather than simply upper or lower limits. Using the light curves of Mrk 421 measured in different X-ray energy bands, Takahashi et al. (1996) performed a cross-correlation analysis and found that the longer relative time lags of the lower energy data versus the higher energy data are consistent with synchrotron cooling of the underlying electron distribution. Several authors have noted this effect and have calculated this temporal dependence for the cases of bursts and blazars (e.g., Tashiro et al. 1995; Tavani 1996; Dermer 1998). Takahashi et al. use the TeV variability time scale (Kerrick et al. 1995) to estimate a Doppler factor and find $\mathcal{D} = 5$ (cf. Takahara 1994). Using this estimate and their time lag measurements, they derive a magnetic field of $B = 0.2$ G. From non-simultaneous data (Shrader & Wehrle 1997), the synchrotron portion of the SED of Mrk 421 peaks at about ~ 130 eV. Using

$$\epsilon_{\text{peak}} = \frac{B}{B_{\text{crit}}} \gamma^2 \mathcal{D} \quad (54)$$

(cf. eq. 45), and $\gamma = (m_p/m_e)\Gamma$, we find $\Gamma \approx 60$ and an observer angle $\theta \approx 5^\circ$. We also obtain an equipartition field strength of $B_{eq} \approx 10n_1^{1/2}$ G implying an equipartition parameter of $\xi_B \sim 10^{-2}$. Although the above value for the bulk Lorentz factor is substantially larger than the mean value of $\langle \Gamma \rangle \sim 10$ found by applying the beaming model to a sample of radio-loud objects (Urry & Padovani 1995), its large value may indicate the special nature of gamma-ray loud blazars which are characterized not only by small observing angles but also by larger than typical bulk Lorentz factors. Despite the crudeness of this calculation, it illustrates the potential applicability of this sort of analysis to blazars as well as bursts.

We thank Jeff Skibo for many useful discussions, and we thank Markus Böttcher for providing us with his computer code for calculating the synchrotron emissivity. This work was performed while J.C. held a National Research Council-NRL Research Associateship and was supported by the Office of Naval Research and the *Compton Gamma-Ray Observatory* Guest Investigator program.

REFERENCES

- Blandford, R. D., & McKee, C. F. 1976, *Phys. Fluids*, 19, 1130
 Costa, E., et al. 1997, *Nature*, 387, 783
 Crusius, A., & Schlickeiser, R. 1986, *A&A*, 164, L16
 Crusius, A., & Schlickeiser, R. 1988, *A&A*, 196, 327
 de Jager, O. C., & Harding, A. K. 1992, *ApJ*, 396, 161
 de Jager, O. C., et al. 1996, *ApJ*, 457, 253

- Dermer, C. D., Miller, J. A., & Li, H. 1996, *ApJ*, 456, 106
- Dermer, C. D., Sturmer, S. J., & Schlickeiser, R. 1997, *ApJS*, 109, 103
- Dermer, C. D., & Chiang, J. 1998, *New Astronomy*, 3, 157
- Dermer, C. D., 1998, *ApJL*, submitted
- Dingus, B. L. 1995, *Ap&SS*, 231, 187
- Djorgovski, S. G., et al. 1997, *Nature*, 387, 876
- Ellison, D. C., Baring, M. G., & Jones, F. C. 1995, *ApJ*, 453, 873
- Frail, D., et al. 1997, *Nature*, 389, 261
- Galama, et al. 1997, *Nature*, 387, 479
- Garcia, M., et al. 1997, *ApJL*, submitted (astro-ph/9710346)
- Goodman, J. 1997, *New Astronomy*, 2, 449
- Katz, J. I. 1994, *ApJ*, 432, L107
- Katz, J. I., & Piran, T., 1997, *ApJ*, 490, 772
- Kerrick, et al. 1995, *ApJ*, 438, L59
- Kouveliotou, C., et al. 1997, *IAU Circ.* 6660
- Lozinskaya, T. A. 1992, *Supernovae and Stellar Winds in the Interstellar Medium* (New York: AIP)
- Mészáros, P. & Rees, M. J. 1992a, *MNRAS*, 257, 29P
- Mészáros, P. & Rees, M. J. 1992b, *ApJ*, 397, 570
- Mészáros, P., Laguna, P., & Rees, M. J. 1993, *ApJ*, 415, 181
- Metzger, M. R., et al. 1997, *Nature*, 387, 878
- Panaitescu, A. & Mészáros, P. 1998a, *ApJ*, 492, 683
- Panaitescu, A. & Mészáros, P. 1998b, *ApJ*, in press (astro-ph/9711339)
- Paczyński, B. 1998, *ApJ*, 494, L45
- Piro, L., et al. 1998, *A&A*, 331, L41
- Press, W. H., Teukolsky, S. A., Vetterling, W. T., & Flannery, B. P. 1992, *Numerical Recipes in FORTRAN* (New York: Cambridge University Press)
- Rees, M. J. 1966, *Nature*, 211, 468
- Rees, M. J., & Mészáros, P. 1992, *MNRAS*, 258, 41P
- Rybicki, G. B., & Lightman, A. P., 1979, *Radiative Processes in Astrophysics* (New York: Wiley-Interscience), p. 179
- Sari, R. & Piran, T. 1995, *ApJ*, 455, L143
- Schaefer, B. E., et al. 1998, *ApJ*, 492, 696

- Shrader, C. R., & Wehrle, A. E. 1997, in AIP Conf. Proc. 410, 4th Compton Symposium, ed. C. D. Dermer, M. S. Strickman & J. D. Kurfess (New York: AIP), 328
- Takahara, F. 1994, in Towards a Major Atmospheric Cerenkov Detector III, ed. T. Kifune (Tokyo: Universal Acad.), 131
- Takahashi, et al. 1996, ApJ, 470, L89
- Tashiro, M., et al. 1995, PASJ, 47, 131
- Tavani, M. 1996, ApJ, 466, 768
- Urry, C. M., & Padovani, P. 1995, PASP, 107, 803
- van Paradijs, J., et al. 1997, Nature, 386, 686
- Vietri, M. 1997, ApJ, 478, L9
- Waxman, E. 1997a, ApJ, 485, L5
- Waxman, E., Kulkarni, S., & Frail, D. A. 1997, ApJ, submitted, (astro-ph/9709199)
- Wijers, R. A. M. J., Rees, M. J., & Mészáros, P. 1997, MNRAS, 288L, 51
- Woosley, S. E. 1993, ApJ, 405, 273

Fig. 1.— Comparison with the analytic result of Dermer & Chiang 1998. The parameters are $\Gamma_0 = 300$, $B = 1$ G, $n_{\text{ext}} = 1$ cm $^{-3}$, $s = 2$. *Upper panel:* The spectra, from top to bottom, are at observer times $t_{\text{obs}} = 1, 10, 10^2, \dots, 10^6$ seconds, with the present calculation plotted as the solid curves and the analytic estimate as the dashed curves. *Lower panel:* Light curves at radio (2.4 GHz, dotted), optical (1 eV, solid), X-ray (1 keV, dashed) and gamma-ray (1 MeV, dot-dashed) energies. The results from the analytic estimate are over-plotted as symbols. Light curves for each successive energy band are displaced vertically by 2 units for clarity.

Fig. 2.— *Upper panel:* Radio surface brightness versus perpendicular distance as a function of observer angle θ at constant time delays, $t_{\text{obs}} = 1, 10, 10^2, \dots$ seconds (top to bottom). *Lower panel:* Apparent size versus time delay. The data points are from the above calculation and the solid curve is equation 39 assuming $\zeta = 3$, i.e., a radiative blast-wave.

Fig. 3.— Numerical results from our blast-wave calculation using model parameters for a burst in equipartition, i.e., $\xi_B = 1$. Other relevant parameters are $\xi_e = 0.5$, $\Gamma_0 = 300$, $E_0 = 10^{52}$ ergs, $n_{\text{ext}} = 1$ cm $^{-3}$, $s = 3$, and $\eta = 1$. *Panel a:* The bulk Lorentz factor of the blast-wave shell as a function of shell radius. The vertical dotted lines indicate the radii of the nearest surface of the shell at observer times $t_{\text{obs}} = 1, 10, 10^2, \dots$ s. The power-law of the bulk Lorentz factor during the deceleration phase is $\zeta \simeq 1.9$. *Panel b:* Synchrotron and synchrotron self-Compton spectra at the above observer times. The spectrum corresponding to each time can be identified by the energy, ϵ_{peak} , of its synchrotron peak which decreases monotonically with time. As in figure 1, the vertical lines denote various observer energies—the dot-dot-dot-dashed line corresponds to 1 TeV. *Panel c:* Co-moving electron distributions at the leading surface of the shell at the above observer times. Each distribution can be identified by the high energy break which corresponds to the synchrotron peak and which also decreases monotonically with time. The dashed curves show our analytic estimate (eq. 42) for these distributions. *Panel d:* Light curves for radio, optical, X-ray, gamma-ray and TeV energies.

Fig. 4.— Burst spectra near ϵ_{peak} for different values of the magnetic field equipartition parameter illustrating the effect of different degrees of synchrotron cooling on the burst spectral shape. In all three cases, the initial bulk Lorentz factor $\Gamma_0 = 260$ (eq. 51). For the solid, dashed and dotted curves we use an electron injection index $s = 4$. *Solid curve:* The spectrum obtained for the limiting value $\xi_B = 5.5 \times 10^{-5}$ (eq. 52) which marks the transition between complete and incomplete electron cooling. The energy spectral indices ($L_\nu \propto \nu^{-\alpha}$) above and below ϵ_{peak} are $\alpha = -1/3$ and $\alpha = s/2 = 2$ respectively. *Dashed curve:* Here $\xi_B = 1 \times 10^{-6}$, and we have $\alpha = (s - 1)/2 = 3/2$ above ϵ_{peak} . *Dotted curve:* $\xi_B = 1 \times 10^{-2}$. Above ϵ_{peak} , $\alpha = s/2 = 2$, and below ϵ_{peak} there is an additional spectral break due to the cooled electrons which have been injected at the lower cut-off energy (eq. 42)—just below ϵ_{peak} , $\alpha = 1/2$ and below the additional break, $\alpha = -1/3$. *Dot-dashed curve:* $\xi_B = 10^{-5}$ and $s = 2$. Just above the low energy break we have $\alpha = (s - 1)/2 = 1/2$, and the νL_ν peak corresponds to emission from the electrons at the high energy cut-off.

Fig. 5.— Burst calculation with $\Gamma_0 = 260$ and $\xi_B = 5.5 \times 10^{-5}$. All other parameters are the same as for figure 3. The thin curve in panel a is the initial estimate of the bulk Lorentz factor using eq. 33. The thick curve is the solution to which our iterative procedure converges. The difference in these curves shows the effect of the electrons not being radiative due to the weak magnetic fields.

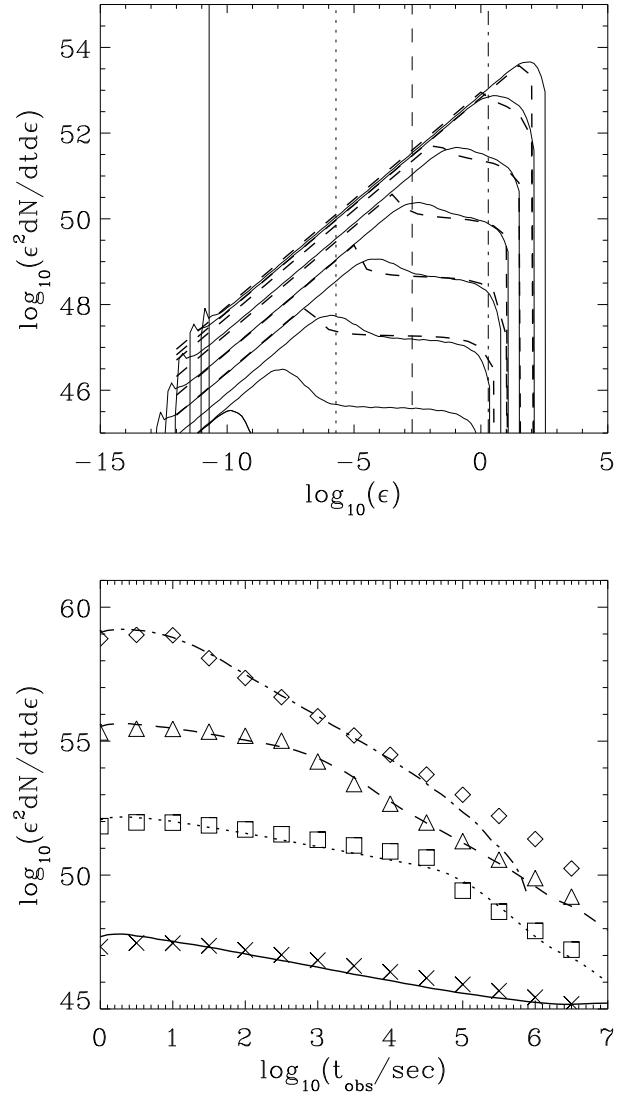


Fig. 1.—

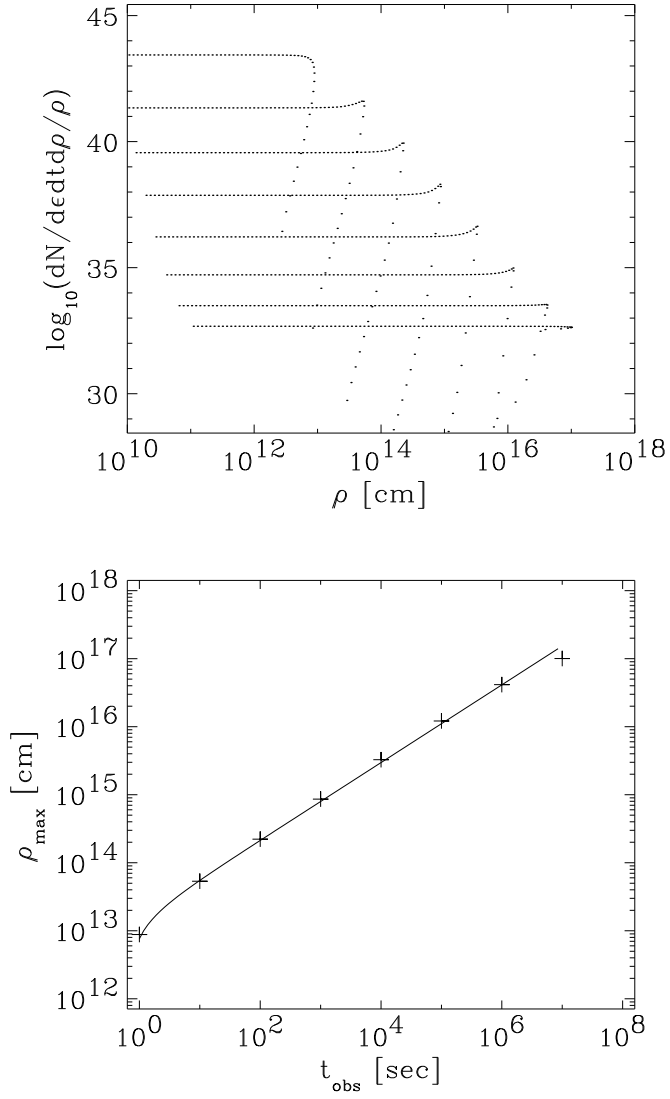


Fig. 2.—

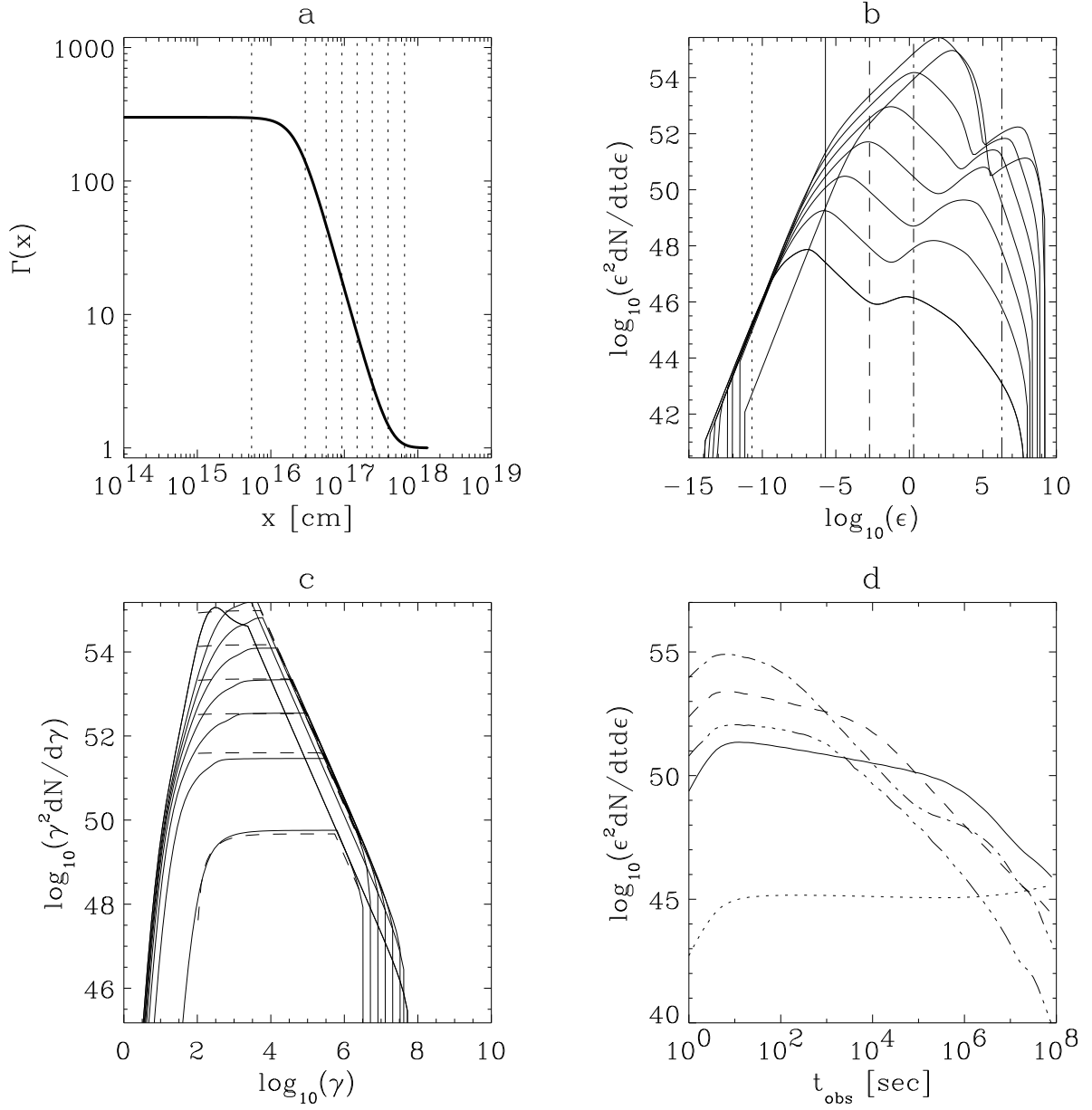


Fig. 3.—

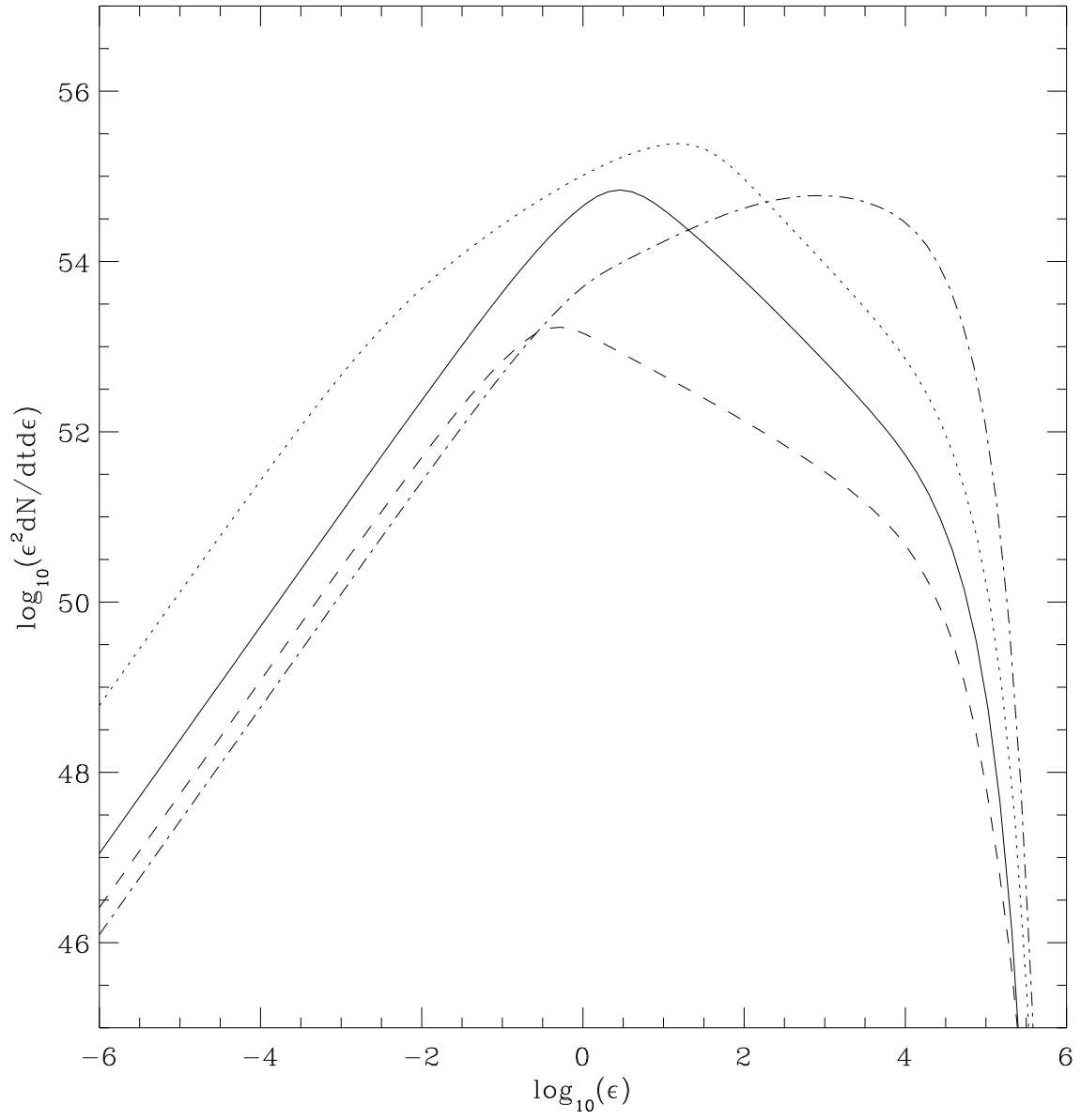


Fig. 4.—

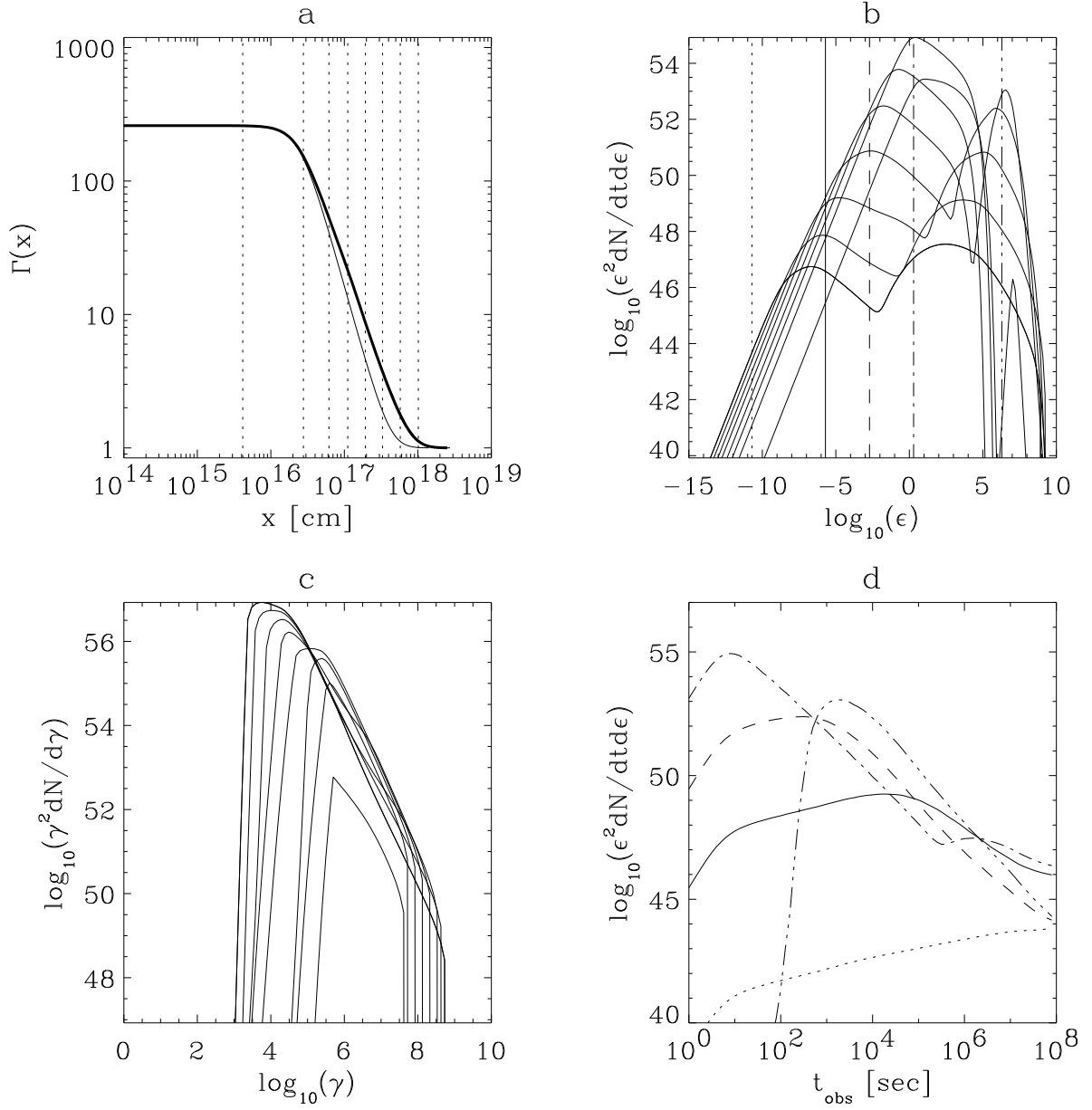


Fig. 5.—